Review of Scientific Instruments

Small-angle neutron polarimetry apparatus (SANPA): Development at the NIST Center for Neutron Research

Cite as: Rev. Sci. Instrum. **90**, 063303 (2019); https://doi.org/10.1063/1.5091110
Submitted: 01 February 2019 . Accepted: 01 June 2019 . Published Online: 26 June 2019

J. Tosado, W. C. Chen, S. Gnewuch, T. Hasaan, T. Dax, and E. E. Rodriguez

AIP Publishing

Review of Scientific Instruments ARTICLE scitation.org/journal/rsi

Small-angle neutron polarimetry apparatus (SANPA): Development at the NIST Center for Neutron Research

Cite as: Rev. Sci. Instrum. 90, 063303 (2019); doi: 10.1063/1.5091110
Submitted: 1 February 2019 • Accepted: 1 June 2019 •
Published Online: 26 June 2019

J. Tosado,[1,a)] W. C. Chen,[2,3] S. Gnewuch,[1] T. Hasaan,[2] T. Dax,[2] and E. E. Rodriguez[1]

AFFILIATIONS

[1] Department of Chemistry and Biochemistry, University of Maryland, College Park, Maryland 20742, USA
[2] NIST Center for Neutron Research, National Institute of Standards and Technology, 100 Bureau Drive, Gaithersburg, Maryland 20899, USA
[3] Department of Materials Science and Engineering, University of Maryland, College Park, Maryland 20742, USA

[a)] **Electronic mail:** jtosado@umd.edu

ABSTRACT

Spherical neutron polarimetry directly measures the rotation of the neutron polarization after scattering from materials with magnetic structure. It is an under utilized measurement technique that is capable of measuring all nine elements of the polarization tensor of a material. In this article, we describe our new cryogen-free small-angle neutron polarimetry apparatus and infrastructure at the NIST Center for Neutron Research. The resulting apparatus is capable of continuous operation and is designed for measurements at low temperatures (4–8 K) using niobium Meissner shielding and mu-metal shielding to produce a zero-field (≤1 μT) cooling sample environment.

I. INTRODUCTION

Complex and exotic states in matter such as cycloidal, helical, or skyrmion lattices can pose unique challenges toward their full characterization. In particular, noncollinear magnetic systems can require specialized instrumentation to fully elucidate the spatial arrangements of the magnetic moments. By further developing new instrumentation and methodologies in neutron scattering, we can resolve such exotic states in crystalline matter.[1] Neutron scattering is uniquely suited for these challenges since the neutron moment is $-1.913\ \mu_N$ and interacts with magnetic moments in solids much more strongly than x-rays. While unpolarized neutron scattering is powerful enough to solve many cases of long-range magnetic ordering, a more specialized technique known as spherical neutron polarimetry (SNP) can unambiguously determine complex types of order in materials such as chiral antiferromagnets,[2] multiferroics,[3,4] superconductors,[5] and magnetoelectrics.[6] We detail the development of new SNP instrumentation at the NIST Center for Neutron Research (NCNR) that takes advantage of existing infrastructure for small-angle neutron scattering (SANS) instrumentation. We call this new set of instrumentation SANPA for small-angle neutron polarimetry apparatus.

In addition to studying energy and momentum transfer during neutron scattering measurements, we can also utilize the neutron's magnetic moment to further resolve certain features in a scattering experiment. By polarizing the incident neutron beam in a precise orientation prior to scattering from the sample, we can successfully untangle certain types of information. For example, with polarized neutrons, we can distinguish scattering due to the nuclear and magnetic cross sections of a sample, separate incoherent from coherent scattering, and assign directionality to different types of modes in inelastic processes (e.g., longitudinal vs transverse fluctuations). Because polarized neutrons can provide extra information upon scattering from condensed matter, its development has been ongoing since the ground breaking polarization experiments of Nathans *et al.* in 1959.[7]

SNP differs from measurements that uniaxially polarize the neutron beam in important ways. With SNP, we can precisely orient the polarization of the incident and scattered neutron beam. The polarization directions, before and after the sample, remain

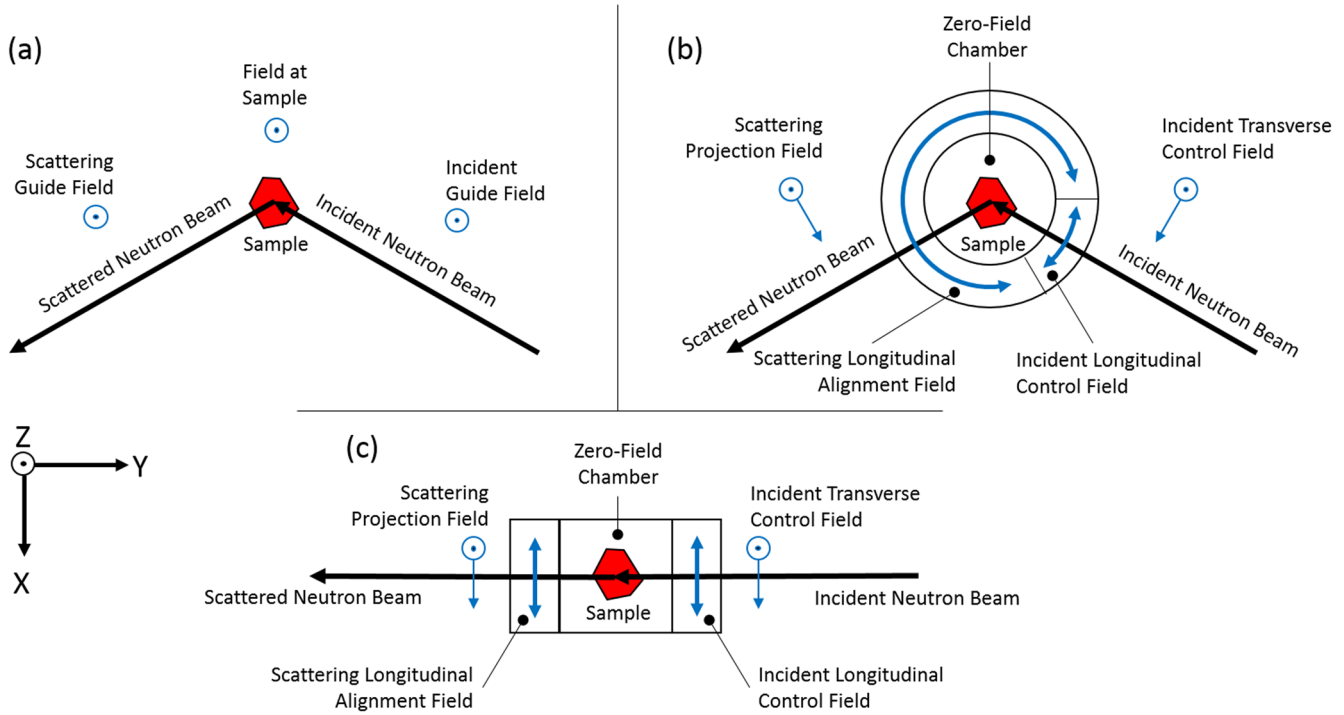

FIG. 1. Illustrated examples as seen from above of (a) the uniaxial polarized beam orientation for the polarization perpendicular to the scattering plane, (b) the spherical neutron polarimetry orientation for a wide-angle apparatus, and (c) the spherical neutron polarimetry orientation for a small-angle apparatus. The scattering plane is parallel with the page. Blue arrows indicate possible magnetic field directions in their respective regions.

independent from one another, and with such a configuration, the experimentalist fully recovers the polarization property tensor of a material.[8–10] In the uniaxial configuration [Fig. 1(a)], one cannot segregate the magnetic fields that align the beam's polarization on the incident side from those that measure the polarization on the scattering side. Without segregation of the fields, the polarization direction must be adiabatically transferred from the region of incidence to the scattering one. As a result, the uniaxial technique measures only projections of the three-dimensional (3D) scattered polarization vector.[11,12] SNP instrumentation overcomes this loss of information through (1) efficient polarization filtering, (2) precise control over magnetic field alignment, (3) creation of a zero-field chamber around the sample, and (4) isolation of the magnetic fields that control the incident beam polarization from those that measure the scattered beam polarization.[13] To highlight the differences between both types of polarization experiments (uniaxial vs SNP), Figs. 1(b) and 1(c) show a schematic of the SNP configuration for wide-angle and small-angle geometries.

While more complex to perform than uniaxial polarization measurements, SNP can involve less modeling of the measurement data, especially in confirming subtle or complex magnetic structures in materials due to its rigorous sampling of a material's full polarization tensor. SNP is fundamentally a 3D measurement of the scattered polarization,[14] and it therefore requires an integrated system of hardware[15] and software[16] to facilitate its usability. The extra complexity arising in SNP experiments has led to the development of a suite of supporting SNP instrumentation and complementary software in addition to the main apparatus.

Currently, three polarimeter designs exist worldwide[15,17–20] and several instruments operate year round that utilize them.[15,17,18,21] Of the three existing SNP designs, two were developed for wide-angle, single crystal diffraction and they are known as CRYOPAD and MuPAD.[15,18,19] In comparison with these wide-angle apparatus, a SANS-type apparatus requires similar infrastructure but is mechanically less complex than its counterparts. The most recent effort in SNP development has been CryoCUP, a compact SNP device for small-angle neutron scattering applications.[20,22]

Our initial effort to develop a compact SNP apparatus has led us to design one free of liquid cryogens that can be integrated into the SANS infrastructure at the NCNR. SANPA is suitable for reactor sources and geared for the measurement of materials whose magnetic structures are characterized by spin-canting or domain inversion. Our design and build of SANPA adds to the existing infrastructure of SNP instrumentation available for the global neutron scattering community. We describe its design, build, testing, and calibration in this review.

II. INFRASTRUCTURE

SNP is inherently a 3D measurement technique that requires precision hardware and a minimum level of automation to make

measurements practical. Consequently, the development of SANPA at NCNR has required the creation of both hardware and software as well as methods for seamless integration into the existing neutron scattering infrastructure. SNP infrastructure can be grouped into three categories: (A) beamline hardware, (B) control hardware, and (C) control software. Beamline hardware refers to any devices subject to neutron irradiation either directly or indirectly. Examples include ^{3}He neutron spin-filters, neutron detectors, and others. Control hardware refers to any devices not purposefully exposed to neutron irradiation, which includes power supplies, metrology hardware, rack hardware, and data acquisition computers. Control software manipulates the hardware in real time, acquires real-time data, and analyzes real-time data. In this section, we describe the state-of-the-art of our infrastructure starting from the sample environment to the neutron polarization control hardware and finally the user interface.

A. Beamline hardware

Since SANPA is specifically for small-angle scattering applications, the analyzing ^{3}He neutron spin-filter does not move relative to the sample environment. This scenario is not true in a wide-angle scattering apparatus. The fixed geometry for SANPA has the effect of keeping the overall design relatively simple when compared to instruments that can accommodate wide scattering angles such as CRYOPAD or MuPAD. As a result, SANPA does not need to account for the rotation of filters and detectors. The seven in-line instruments depicted in Fig. 2 comprise the beamline hardware, and they are as follows:

1. ^{3}He neutron spin-polarizing filter: This is a Spin-Exchange Optically Pumped (SEOP) ^{3}He cell with vertical polarization.[23] This device acts on the unpolarized neutron beam by absorbing antiparallel spin-states producing a beam polarized in one spin-state.[24]
2. Incident transverse rotator: This four coil electromagnet produces a field that controls the polarization of the incident neutron beam. It adiabatically rotates the polarization within the transverse XZ-plane. Refer to Fig. 3(b) for an illustration.
3. Incident longitudinal rotator: This single coil solenoid produces a field that rotates the neutron polarization. As such, the polarization rotates through the longitudinal YZ-plane. In the SNP literature, this device is sometimes referred to as the nutator.
4. Zero-field chamber: This enclosure, shaped by the inner and outer Meissner shields, houses two of the rotators and the sample itself. When fully assembled, the chamber's volume is set by the inner Meissner shield and provides a zero-field environment for the sample. Refer to Fig. 3(a) for an illustration.
5. Scattering alignment rotator: This single coil solenoid produces a field that selects the measurement axis of the neutron beam polarization. Much like device (3), it also rotates the polarization through the longitudinal YZ-plane. Unlike (3), however, this rotator's purpose is to align the desired polarization component to be measured with the magnetic field direction of the next device (6). In the previous SNP literature, this rotator is also often referred to as a nutator.
6. Scattering transverse projector: This four coil electromagnet produces a field that filters the polarization component to be measured. Only the desired component of the polarization aligned with the transverse directed magnetic field can be projected out to the next device (7). Refer to Fig. 3(b) for an illustration.
7. ^{3}He neutron spin-analyzing filter: This is a SEOP ^{3}He cell with longitudinal polarization.[23] This device acts on the scattered neutron beam by absorbing antiparallel spin-states in the beam leaving the remaining fraction of spin-up or spin-down states to be detected.

The incident longitudinal rotator (3), the zero-field chamber (4), and the scattering alignment rotator (5) comprise the zero-field sample environment (see Fig. 2). Our zero-field sample environment is an adaptation of the CRYOPAD design[15] to fit within the space restrictions of NCNR scattering infrastructure. As with CRYOPAD, we too take advantage of the Meissner effect via superconducting niobium foil. We shaped the Nb foil to completely separate magnetic fields used for measurement (located on the scattering side) from those used for control (located on the incident side); see Fig. 1(c). Our design uses two overlapping layers of niobium foil (0.8 mm thickness). The niobium foil has been spot-welded into two rectangular cuboid containers, which are fitted one inside the another. Each container is rectangular but open on one side so that 5 of the 6 sides are closed. The shield placement is estimated to be within

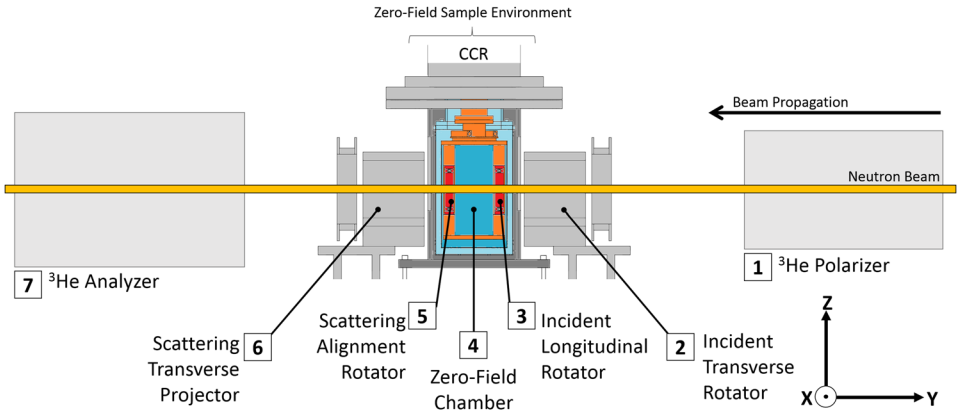

FIG. 2. Beamline hardware viewed from the side: (1) ^{3}He neutron spin-polarizer, (2) incident transverse rotator, (3) incident longitudinal rotator, (4) zero-field sample chamber, (5) scattering alignment rotator, (6) scattering transverse projector, and (7) ^{3}He neutron spin-analyzer.

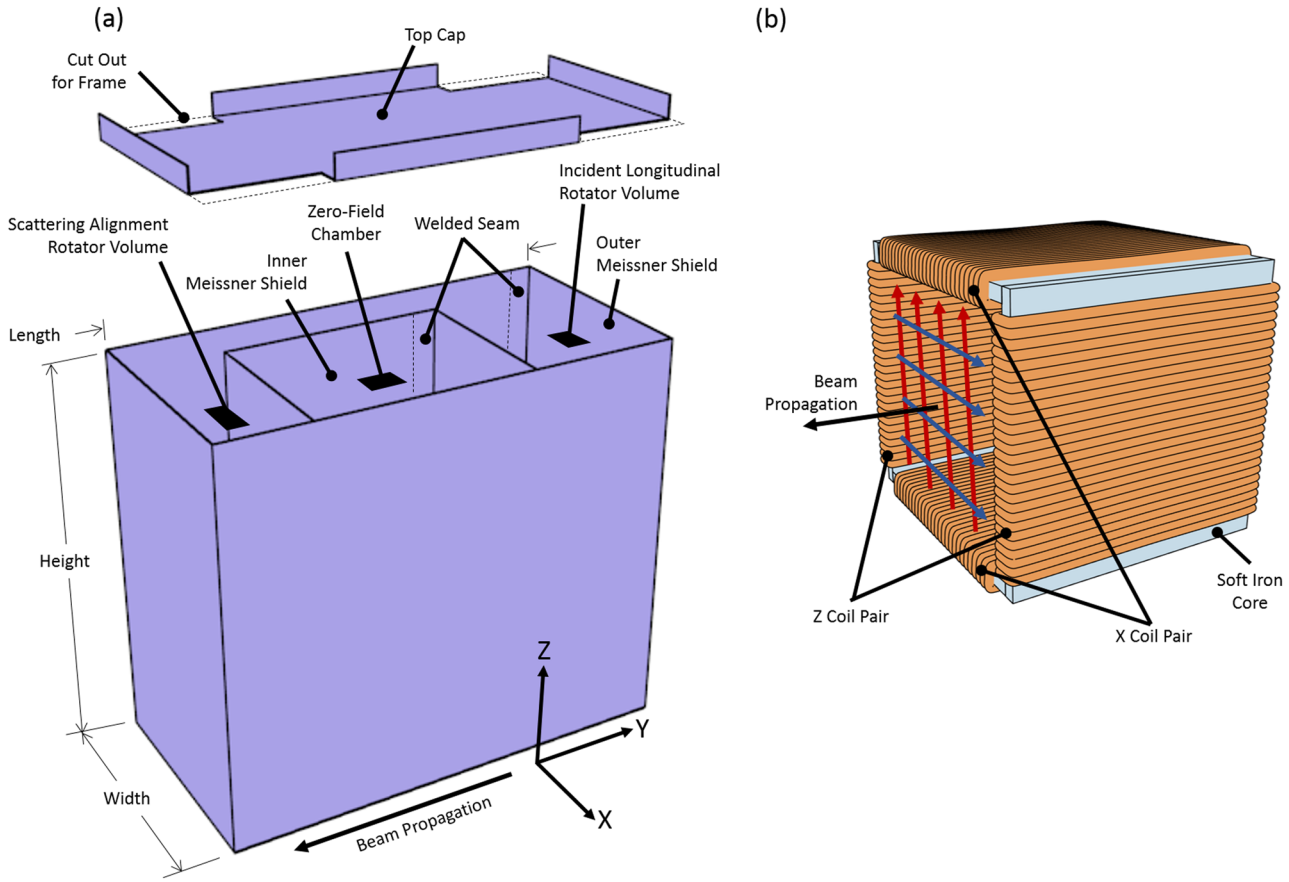

FIG. 3. (a) Illustration of the Meissner shield construction. The length, width, and height of the outer shield are 101.6 × 76.2 × 152.4 mm^3. The inner shield is 63.5 × 76.2 × 146.0 mm^3. (b) Illustration of the transverse rotator (2) and projector (6). Red arrows indicate the magnetic field produced by the Z coil pair, and blue arrows indicate the magnetic field produced by the X coil pair. The length, width, and height are 101.6 × 114.3 × 114.3 mm^3.

a nominal ±0.5 mm of the design specifications. We refer to the two shields as the inner shield and the outer shield, respectively. The inner and outer shields are welded together and have a single removable cap that allows samples to be installed. This nesting creates a fully enclosed inner volume and two outer volumes. The inner volume comprises the zero-field chamber (4) where samples are mounted. The two outer volumes, which lie between the inner and outer shields, enclose the longitudinal rotator (3) and the alignment rotator (5). In this configuration, the outer shield separates the controlling magnetic field generated by the transverse rotator (2) from the measurement field generated by the transverse projector (6). It also separates the controlling magnetic field generated by the longitudinal rotator (3) from the measurement field generated by the alignment rotator (5).

Both the alignment rotator (5) and longitudinal rotator (3) are identically constructed solenoids (15 × 47.6 × 65.9 mm^3). These solenoids are within a millimeter of the shielding and thermally connected to it. They have been constructed from a superconducting copper clad niobium wire (Supercon 338M-141B1B) to limit heating effects from applied current. The copper has been stripped from the part of the wire used in wrapping the solenoid and is electrically insulated with polytetrafluoroethylene. By calculating from the Biot–Savart law the magnetic field generated by each solenoid over the volume of the solenoid, we expect that the resulting magnetic fields generated are nominally horizontal and uniform to within ±6 μT in the path of the beam (1 × 1 cm^2 cross section).

When compared to CRYOPAD, our zero-field sample environment is distinct in two ways. First, to maintain superconductivity, a high powered closed cycle refrigerator (CCR) is used to cool the shielding and solenoids down to a nominal 3.5 K as opposed to using a liquid cryogen bath. Using a CCR removes the need to refill liquid cryogens thereby allowing continuous uninterrupted measurement. The second distinction is that the entire sample environment is thermally grounded to the same CCR system. Material samples, in our case, are then limited to a temperature sufficiently less than the superconducting transition of niobium. We therefore limit the operating temperature range to within a nominal 4–8 K (refer to Sec. III). While the sample environment design is not optimal for experiments which require a wider temperature range, we

anticipate to integrate new sample environments in future upgrades of SANPA.

Mounted on either side of the zero-field sample environment are the transverse rotator (2) and the transverse projector (6). These two devices are also identically constructed. Each is comprised of two pairs of copper coils where each coil is wrapped around one of the four soft iron plates. The plates are mounted and magnetically connected in a four-sided cubic configuration; see Fig. 3(b). A pair of coils, when energized, generates one component of either a horizontal or a vertical magnetic field. Both coils, when energized, create a net magnetic field within the transverse plane (the XZ-plane of Fig. 2). A static field with constant magnitude can be uniformly rotated by choosing directional cosine component currents through the coil pairs. The transverse rotator (2) and the transverse projector (6) are each adiabatically coupled to the ^{3}He polarizer (1) and analyzer (7), respectively, via longitudinal guide field devices not depicted in Fig. 2. For a thorough description of the polarizing and analyzing filters, we refer the reader to Refs. 23 and 25.

B. Control hardware

The control hardware serves to energize the beamline hardware and responds to safety limits and user initiated commands. This set of instrumentation consists of five power supplies, a control relay, and a computer workstation. Two of the power supplies mentioned are integral to the operation of the ^{3}He spin-filters, and we again refer to Refs. 23 and 25 for that description. The remaining three power supplies are single pole, dual channel, semi-automatic power supplies (Sorensen XPF 60-20DP). Since all the power supplies described here are both single pole and require manual disengagement, the powers supplies are interfaced with a custom control relay system that allows automatic engagement and disengagement as well as polarity switching. This level of automation is key for safe continuous operation of the beamline hardware. Automation allows applied currents to be limited or automatically switched off in the event of coil quenching or user error and promotes an intrinsically safe system.[26]

C. Control software

Within an international user facility like NCNR, diverse scientific teams require access to a particular experimental workstation. From this perspective, the established hardware and software infrastructure acts as a substrate for experimenters. It is therefore advantageous, in the development of new infrastructure, to make as few permanent modifications to the facility infrastructure as possible. This strategy will also help transfer of SANPA to another neutron source such as the high-flux-isotope reactor (HFIR). At the scale of SNP instrumentation, much of the hardware is required to be removable and SANPA is therefore all modular in design. Seamlessly integrating already modular SNP instrumentation into existing infrastructure then relies on a highly conformable software infrastructure that impermanently integrates into a specific beamline workstation for the duration of an experiment.

The NCNR software infrastructure reflects a set of well tested hardware control and data acquisition methods. This infrastructure provides a highly reliable system for error handling, data backup, and storage and is customized to each beamline workstation. Our SANPA software infrastructure must then adapt to the subset of different workstations on which SNP experiments will take place. For that reason, we have chosen to use the Labview™ programming environment to develop our control and data acquisition software. The Labview programming environment is known for rapid software development within scientific settings.[27] The resulting software format interface discussed here is thus modeled after the Nanonis™ control software interface.[28,29] This model of user interface renders key experimental parameters and controls within the software as global variables that can be logged or called on in a modular fashion. The effect is a "plug-and-play" experimental software environment suitable for integrating additional metrology or control hardware by using standard drivers.

The SANPA control software, installed on a mobile Windows™ based workstation computer, operates through two main communication pathways. The first pathway is through traditional serial, general purpose interface bus (GPIB) and universal serial bus (USB) interfacing. The second is through the TCP/IP protocol under a client-server model. The first pathway allows communication with all modular control hardware unique to the SNP infrastructure. For example, our control relay, power supplies, temperature controller, vacuum pump, and all other metrology hardware, which may be needed for a given experiment, are connected through either GPIB or USB. Through this pathway, software coordinates engagement and polarity changes, receives data from temperature and vacuum pump controllers, and executes real-time safety protocol. The second pathway communicates with NCNR data acquisition and control software, and it is this pathway which allows for seamless integration. Here, the SANPA control software communicates as a client. Then, for a given beamline workstation, a generic driver runs locally at that workstation as a server. This server interprets client requests as user generated commands to execute established NCNR functionality thereby taking advantage of established NCNR error handling methods. It also permits the streaming of data back to the SANPA workstation computer for customized, real-time data visualization and backup storage from anywhere within the NCNR network. The key to using the client-server model is that the client is generally not concerned with internal server processes. This allows the SANPA control software infrastructure to be quickly connected and disconnected from the NCNR software during or at the conclusion of an experiment.

III. OPERATION

The unpolarized neutron beam enters from the right of Fig. 2 emerging through a monitor and undergoes a seven step process prior to absorption by the detector. Each of these seven steps corresponds to the seven components denoted in Fig. 2. These seven steps fully characterize the operation of the apparatus and are enumerated as follows:

Step 1. In this first step, the unpolarized beam is polarized by our ^{3}He polarizer (1). Let this initial polarization be vertical and characterized by the vector $\mathbf{P}_z = (0, 0, P_z)$ directed along the Z-axis, where P_z is the magnitude of the beam polarization determined by using the ^{3}He polarizer (1).

Step 2. The polarization of the beam is then adiabatically transported to the transverse rotator (2). Here, the beam polarization is directed to an angle θ_1 about the Y-axis within

the XZ-plane transverse to the beam propagation. Let this operation be represented by the rotation operator $\mathbf{R}_T(\theta_1)$, which is a 3 × 3 rotation matrix about the Y-axis.

Step 3. The beam then crosses through the outer Meissner shield and passes through the horizontal magnetic field of the longitudinal rotator (3). This field precesses the beam polarization through the longitudinal plane (the YZ-plane of Fig. 2) to an angle ϕ_1. Let this operation be represented by the rotation operator $\mathbf{R}_L(\phi_1)$, which is a 3 × 3 rotation matrix about the X-axis.

Step 4. As the beam crosses the inner Meissner shield, the polarization is set to $\mathbf{P}_{\text{in}}$ and enters the zero-field chamber (4). With a sample of some magnetic structure in place, the incident beam scatters from it to be modified by the polarization property tensor, $\mathbf{T}$, for that material, resulting in the scattered beam polarization, $\mathbf{P}_{\text{out}}$, that then emerges from that sample, i.e.,

$$\mathbf{P}_{\text{out}} = \mathbf{T} \quad \mathbf{P}_{\text{in}}. \tag{1}$$

Step 5. The scattered beam leaves the zero-field chamber (4) by again crossing through the inner Meissner shield to enter the horizontal magnetic field of the scattering alignment rotator (5). While in this field, the beam polarization precesses by an angle ϕ_2, again within the longitudinal plane, so as to align the desired component of the beam polarization to be measured with the field of the transverse projector (6). Let this operation be represented by the rotation operator $\mathbf{R}_A(\phi_2)$, which is a 3 × 3 rotation matrix about the X-axis.

Step 6. The aligned polarization, after crossing the outer Meissner shield, enters the magnetic field of the transverse projector (6) whereby, through precession within this field, the desired component of the beam polarization to be measured, P_j, is projected out. Let this operation be represented by a dot product operation of the scattered polarization with the vector $\mathbf{B}(\theta_2) = [\sin(\theta_2), 0, \cos(\theta_2)]$, i.e.,

$$P_j = \mathbf{B}(\theta_2) \cdot \mathbf{P}_{\text{out}}. \tag{2}$$

Step 7. The projected beam polarization, P_j, which is the component of $\mathbf{P}_{\text{out}}$ to be measured, is then adiabatically transported to the ^{3}He analyzer (7). The ^{3}He analyzer then spin-analyzes the projected beam polarization, P_j, where the filter is characterized by I, the maximum measurable intensity of the polarized beam. The analyzed beam is then absorbed by using the detector to produce a single measurement.

For a given P_j, two measurements are made, one of spin-up states and one of spin-down states. The polarization of that component is then calculated, i.e.,

$$P_j = \frac{I_+ - I_-}{I_+ + I_-}, \tag{3}$$

where I_+ and I_- are the number of spin-up and spin-down states measured, respectively. With this in mind, the operation of the apparatus can now be understood by writing Eq. (2) in terms of the constituent operators, i.e.,

TABLE I. Angles required for measuring the ith and jth tensor elements.

(i, j)	θ_1	ϕ_1	θ_2	ϕ_2
XX	$\pi/2$	0	$\pi/2$	0
YX	0	$-\pi/2$	$\pi/2$	0
ZX	0	0	$\pi/2$	0
XY	$\pi/2$	0	0	$\pi/2$
YY	0	$-\pi/2$	0	$\pi/2$
ZY	0	0	0	$\pi/2$
XZ	$\pi/2$	0	0	0
YZ	0	$-\pi/2$	0	0
ZZ	0	0	0	0

$$P_j = \mathbf{B}(\theta_2) \cdot \left[\mathbf{R}_A(\phi_2) \quad \mathbf{T} \quad \mathbf{R}_L(\phi_1)\mathbf{R}_T(\theta_1)\right] \quad \mathbf{P}_z, \tag{4}$$

and after passing through the ^{3}He analyzer, the intensity measured at the detector can be described in terms of the maximum measurable intensity,

$$I_\pm = \frac{1}{2} I(1 \pm P_j). \tag{5}$$

If one ignores both the magnetic and nuclear-magnetic interactions of a material sample, then from Eq. (4), there are only two distinct operations being performed on the initial polarization $\mathbf{P}_z$. The first is generally a net rotation of the initial state polarization characterized by the operation sequence $\mathbf{R}_A$, $\mathbf{T}$, $\mathbf{R}_L$, and $\mathbf{R}_T$. The second is a projection of that rotated polarization by the transverse projector (6) magnetic field, $\mathbf{B}$. In this way, the magnetic fields used to rotate the beam polarization before and after scattering (i.e., $\mathbf{R}_L$ and $\mathbf{R}_T$, and $\mathbf{R}_A$, respectively) are physically distinct from the one used to filter it (i.e., $\mathbf{B}$).

The final goal of operation is to determine the polarization property tensor, $\mathbf{T}$, of a material. From Eq. (2), it can be seen that if $\mathbf{P}_{\text{in}}$ is set to a Cartesian direction, then each component of $\mathbf{T}$ is equivalent to a measurement of each component of $\mathbf{P}_{\text{out}}$ for that Cartesian direction. The nine components of $\mathbf{T}$ are then (for i, j = 1, 2, or 3; X, Y, or Z)

$$T_{ij} = P_j(\{\theta_1, \phi_1\}_i, \{\theta_2, \phi_2\}_j), \tag{6}$$

where the set of angles $\{\theta_1, \phi_1\}_i$ and $\{\theta_2, \phi_2\}_j$ corresponds to the ith direction of $\mathbf{P}_{\text{in}}$ and the jth direction of P_j, respectively. As Cartesian directions are mutually orthogonal, the ith and jth sets are composed of angles equal to 0 or $\pi/2$. Table I shows this relationship for each matrix element denoted by (i, j) with the angular set needed for that measurement.

IV. CALIBRATION

Calibration of SANPA was performed on the PHADES beamline at the NCNR [flux, 2×10^6 n/cm^2/s; wavelength 0.41001(5) nm]. Calibration begins with characterization of the magnetic shielding. Using a custom cryogenic flux magnetometer in place of a material sample,[30–33] the zero field chamber (4) is cooled to ≈4 K inside a Conetic™ mu-metal box[34] where the net field strength is ≤1 μT. On the application of an external magnetic field,

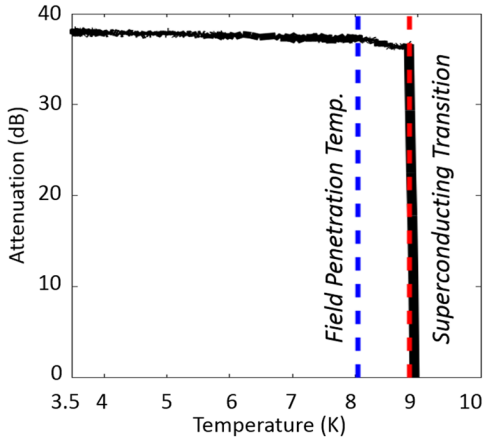

FIG. 4. Measurement of the shielding factor with increasing shield temperature. Black curve: The shielding factor in decibels. Blue dashed curve: The beginning of magnetic field penetration through the shield at about 8 K. Red dashed curve: Superconducting transition of the shield at about 9 K.

ranging from zero to 2 mT, the response of the magnetometer is measured and then compared to the response under equivalent conditions without the niobium shielding in place. Figure 4 shows the shielding factor in decibels as a function of increasing shield temperature. The low temperature shielding factor of about 38 dB first experiences a slight drop at around 8 K and then suddenly drops to zero above 9 K. This is in agreement with the nominal superconducting transition temperature of niobium, which occurs at about 9.3 K.[35] The initial slight drop, we believe, is due to uneven warming of the shield manifesting as an apparent lower transition temperature.

Having this clear indication that the magnetic shielding is properly in place, we first demonstrate control of the neutron beam polarization by precession of it with both the incident longitudinal rotator (3) and the scattering alignment rotator (5). Figures 5(a) and 5(b) show independent control with each of these two solenoids. From a fit to these curves, we convert amperes to radians (0.342 A/rad.) thereby allowing angular positioning of the neutron beam polarization through the longitudinal YZ-plane of Fig. 2.

The next step is to align the axis of incidence, defined by the angles (θ_1, ϕ_1), with the axis of measurement, defined by the angles (θ_2, ϕ_2). This is an iterative process performed without a material sample to scatter from so that, in place **T**, the identity operator is used. The axis of measurement, now described by the operators $\mathbf{B}(\theta_2) \cdot \mathbf{R}_A(\phi_2)$, is rotated through three orthogonal planes, namely, the XY, XZ, and YZ-planes. As the measurement axis is rotated within a plane, for a given angle, the axis of incidence described by the operators $\mathbf{R}_L(\phi_1)\mathbf{R}_T(\theta_1)$ is set in sequence to the +X, +Y, and +Z directions. Three separate measurements of the polarization corresponding to each direction are automatically combined and plotted as vectors in 3D space. Figure 6 shows the resulting three plane measurements. With each plane measurement, the data are modeled with Eq. (4) and a misalignment angle is calculated and applied within the software. This cycle is then repeated until consecutive changes in the data are close to the theoretical noise level.[36]

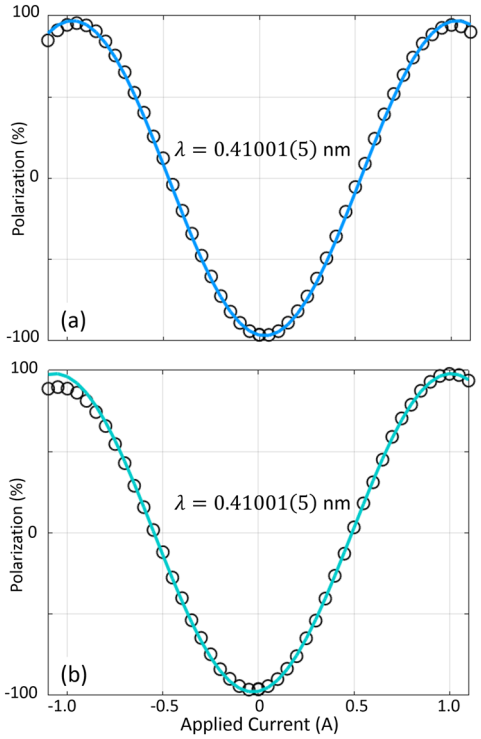

FIG. 5. The change in the neutron beam polarization of (a) the incident longitudinal rotator (3), $\mathbf{R}_L$, and (b) the scattering alignment rotator (5), $\mathbf{R}_A$. Black circles show the response of the polarization with the application of current. The solid blue curves are cosine fits to the data.

The data presented in Fig. 6 should ideally lie on a circle although noise in a single measurement is expected due to the Poisson counting error. Moreover, each data point in Fig. 6 is a vector of three components or six measurements of up and down states thereby compounding that Poisson error.[36] Consequently, after electromechanically correcting for axis misalignment, as just described, the data are still expected to deviate from the circle. Deviations that are greater than the compounded Poisson error are regarded as distortions. We characterize two types of distortions, angular and radial within the plane. Out of plane distortions are discussed in Sec. V. For the data presented in Fig. 6, the average radial distortion is small, less than 1% polarization above the noise. By contrast, the average angular distortion in the YZ and XY-planes was found to be about 8°, which was due to a residual misalignment of the transverse rotator (2) at the time the data were taken.

We first correct for angular distortions. This is a procedure which first involves calculating the set of polar angles, $\{\alpha_k\}$, from the set of planar vectors, $\{\mathbf{P}_k\}$. Each α_k then corresponds to an expected angle, β_k, set by the control software such that the resulting distortion is

$$\delta_k = \alpha_k - \beta_k. \tag{7}$$

To apply this to an arbitrary measurement, we linearly interpolate between angles such that for an arbitrary measured angle, γ,

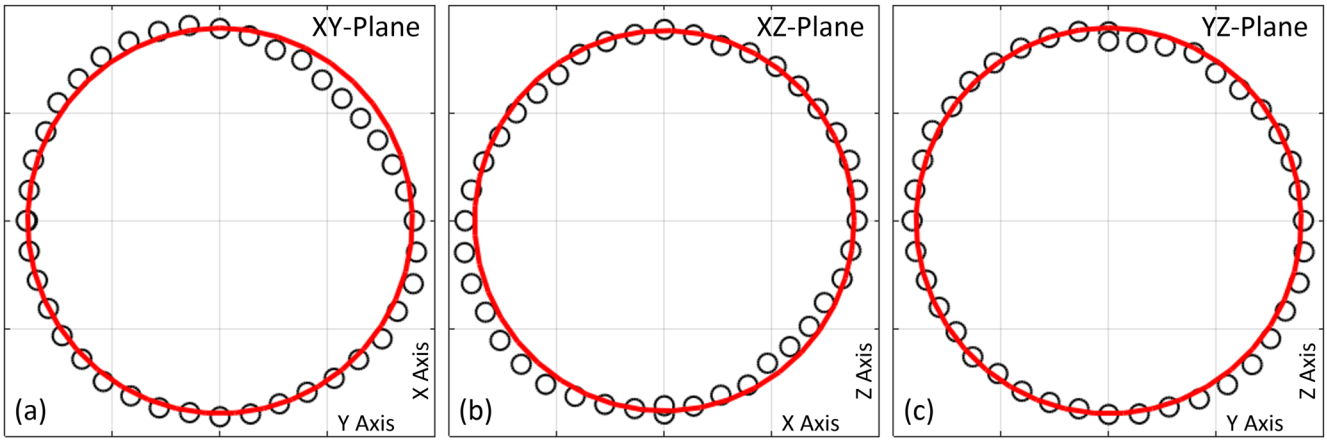

FIG. 6. Rotation of the measurement field within the three cardinal planes. The black circles each represent a measurement in that radial direction within the respective plane. The large red circle in each plane shows the average 89% polarization, whereas the bounding boxes lay at a polarization of 100%. (a) XY-plane. (b) XZ-plane. (c) YZ-plane.

which is in the interval $\alpha_k \le \gamma \le \alpha_{k+1}$, the distortion for that angle is

$$\Delta = \left|\frac{\gamma - \alpha_k}{\alpha_{k+1} - \alpha_k}\right|(\delta_{k+1} - \delta_k) + \delta_k. \tag{8}$$

The corrected angle for an arbitrary measurement is then

$$\Theta = \gamma - \Delta. \tag{9}$$

With the angular distortion from the calibration data removed, correcting for radial distortion is more straightforward. This is accomplished by describing the set of magnitudes, $\{P_k\}$, of the calibration data with a Fourier series, i.e.,

$$P_k(\Theta_k) = \sum_{n=0}^{N/2}[a_n\cos(2\pi\omega_n\Theta_k) + b_n\sin(2\pi\omega_n\Theta_k)], \tag{10}$$

where Θ_k is the kth polar angle of the plane, a_n and b_n are then the coefficients of the expansion, and ω_n are the polar frequencies. This procedure allows us to easily interpolate between the discrete points of our calibration data. A correction to an arbitrary measurement, P_{measured}, with polar angle Θ is then

$$C(\Theta) = \sum_{n=1}^{N/2}[a_n\cos(2\pi\omega_n\Theta) + b_n\sin(2\pi\omega_n\Theta)] \tag{11}$$

such that

$$P_{\text{corrected}} = P_{\text{measured}} - C. \tag{12}$$

V. DISCUSSION AND CONCLUSIONS

With a sample in place, the components of the data points of Fig. 6, which intersect the vertical and horizontal axes in each plane, would then refer to the tensor elements, T_{ij}. Without a sample, the elements T_{ij} correspond to elements of a 3 × 3 identity matrix. Indeed, the data of Fig. 6 produce the following matrix:

$$\mathbf{T}_o = \begin{bmatrix} 0.90(1) & -0.04(1) & -0.02(1) \\ -0.04(1) & 0.89(1) & 0.01(1) \\ 0.02(1) & 0.01(1) & 0.87(1) \end{bmatrix} \times 100\%, \tag{13}$$

which would then be used to correct tensor measurements of samples. With $\mathbf{T}_o$ normalized to the maximum T_{11} element, its discrepancy from the identity matrix is about 2.2%. This close agreement allows the measurement of magnetic reflections over a variety of sample orientations about the X-axis, orientations that yield a polarization above the off diagonal variation of ±2.7% polarization.[10] The slight discrepancy of $\mathbf{T}_o$ suggests that there may be some residual depolarizing process within the apparatus possibly due in part to residual misalignment. Identifying variation in the calibration data at the two percent level requires a more detailed consideration of the out-of-plane components not observable from Fig. 6, a strategy we address elsewhere.[37] However, the type of calibration described above is at least sufficient for small-angle neutron scattering where the coordinate system does not change with the sample orientation, i.e., the coordinate system used for measuring Fig. 6 is fixed to the lab frame, as is implied in Fig. 2.

Even so, our future aim is to construct a wide scattering angle apparatus within our newly developed infrastructure. In this context, the coordinate system becomes fixed to the scattering vector, which is defined as the change in momentum of the beam on scattering. As a result, the coordinate system will continuously change with sample orientation effectively rotating the calibration planes of Fig. 6 about the Z axis. This implies that for a wide-angle apparatus, fully accounting for out-of-plane components should at least be considered during calibration. In anticipation of this requirement, we have extended our range of measurement to cover the sphere. Figure 7(a) shows a 3D plot of this extended measurement field of 1024 vectors or an equivalent 6144 measurements with a continuous experimental time of more than 20 h. Long experimental times like this demonstrate the need for reliable uninterrupted automation of the thousands of power supply changes and the continual safety monitoring of equipment. In addition to having undergone electromechanical calibration, it was necessary to correct the data of Fig. 7 for the neutron polarization time-dependence from both the ^{3}He polarizer (1) and analyzer (7). The data were then normalized to the maximum. After this, variation in the data of Fig. 7 is still evident. Although, with this data viewed from directly along the Y-axis at either of two opposing hemispheres, as in Figs. 7(b) and 7(c), it is

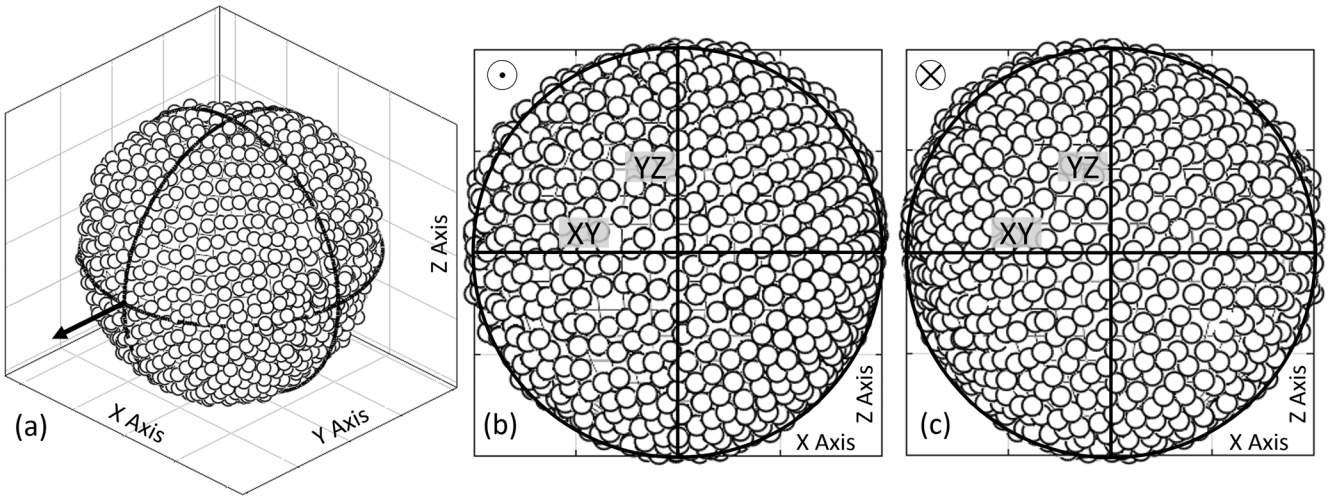

FIG. 7. (a) Normalized, 3D plot of the spherical measurement field. Great circles outline the intersection of three planes with the field. [(b) and (c)] The measurement field projected onto the XZ-plane as seen from two orientations. Black circles and vertical and horizontal lines outline the XZ, YZ, and XY-planes, respectively. The black arrow in (a) is parallel with the beam propagation and is depicted in the top left corner of (b) and (c) for perspective. The bounding boxes lie at a polarization of 100%.

difficult to see from these plots if the variation has structure. To gain more insight, Fig. 8 shows a Mollweide projection of the data. In this map, a triangulation of the data produces a colored surface mapping over the range of the extrema. The great circles depicted in Fig. 7(a) are outlined in Fig. 8 to give perspective. The data visible in Fig. 7(b) are located within the circle labeled XZ, whereas the data visible in Fig. 7(c) are located around this circle.

For spherical polarimetry measurements, only points that intersect the X, Y, and Z axes of the spherical measurement field directly affect tensor measurements and a determination of $\mathbf{T}_o$ should correct for minor variation. The key thing to note from Fig. 8 is that there is less variation along the great circles than in other directions and this out-of-plane data provides additional information toward identifying and reducing any systematic variation that may be present. As an example, we believe that the variation seen in Fig. 8 is mainly due to residual misalignment. By monitoring the spherical field through repeated measurement, we were able to identify the high and low regions in the data as being related to distortion brought on by remnant magnetization in the soft iron cores used with the transverse rotator (2) and projector (6). The remnant magnetization manifests as a distortion of the measurement coordinate system to a nonorthogonal basis, which we attempt to compensate for electrically. Certainly, from Fig. 8, our compensation is not perfect, which indicates that our use of soft iron in this initial design is not ideal, a fact that would have been more difficult to uncover through plane measurement alone. As a result, our next step will be to test a transverse rotator/projector that uses higher permeability cores such as mu-metal.

In conclusion, we have demonstrated our SNP infrastructure as a fully operating measurement and data collection system. SANPA is

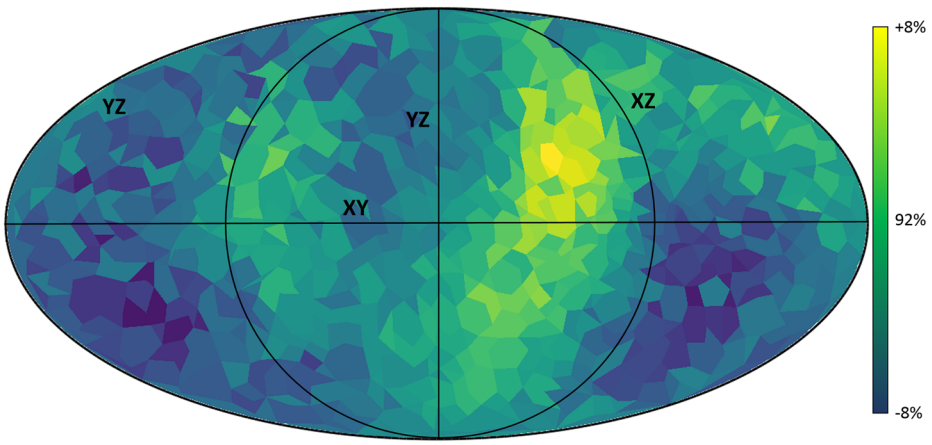

FIG. 8. Mollweide projection of the 3D measurement field depicted in Fig. 7. The black arcs and lines labeled as XZ, YZ, and XY correspond to the intersection with the XZ, YZ, and XY-planes, respectively. The arrow depicted in Fig. 7(a) is pointing out of the page at the center of this plot. The color scale is centered around the average polarization of 92%.

cryogen free, using superconducting solenoids for polarization control over the full 360° of the sphere and superconducting niobium for magnetic shielding on the order of 38 dB with a background that is ≤1 μT. While the infrastructure presented here has been constructed around NCNR infrastructure, we expect that our methods could be easily mapped onto other facilities such as HFIR. Having this foundation laid, the next step will be to add wide scattering angle capabilities suitable for single crystal diffraction. These efforts are already underway, and we expect to begin calibration by the beginning of 2020.

ACKNOWLEDGMENTS

This work was funded by the Department of Energy, Basic Energy Sciences Project, Award No. DE-SC0016434.

Certain commercial entities, equipment, or materials may be identified in this document in order to describe an experimental procedure or concept adequately. Such identification is not intended to imply recommendation or endorsement by the National Institute of Standards and Technology, nor is it intended to imply that the entities, materials, or equipment are necessarily the best available for the purpose.

Throughout this paper, error bars and uncertainty represent one standard deviation.

The manufacturing of parts was through the Mechanical Development Group at the University of Maryland: Dave Cogswell, Bruce Lee, and Jack Touart. The manufacturing of parts was shared with the NCNR Mechanical Engineering Technicians: Doug Johnson, Patrick Connelly, and Scott Slifer. We would also like to acknowledge support from the Center for Nanophysics and Advanced Materials at the University of Maryland: Dr. Johnpierre Paglione, Dr. Steven Anlage, and Dr. Ellen D. Williams.

REFERENCES

[1] L. Coates, H. B. Cao, B. C. Chakoumakos, M. D. Frontzek, C. Hoffmann, A. Y. Kovalevsky, Y. Liu, F. Meilleur, A. M. dos Santos, D. A. A. Myles, X. P. Wang, and F. Ye, Rev. Sci. Instrum. **89**, 092802 (2018).

[2] V. Dmitriev, D. Chernyshov, S. Grigoriev, and V. Dyadkin, J. Phys.: Condens. Matter **24**, 366005 (2012).

[3] A. Poole, B. Roessli, O. Zaharko, and K. W. Kramer, J. Phys.: Condens. Matter **23**, 266004 (2011).

[4] P. Babkevich, L. Testa, K. Kimura, T. Kimura, G. S. Tucker, B. Roessli, and H. M. Ronnow, Phys. Rev. B **96**, 214436 (2017).

[5] M. Schneider, O. Zaharko, U. Gasser, A. Kreyssig, P. J. Brown, and P. C. Canfield, Phys. Rrev. B **74**, 104426 (2006).

[6] P. J. Brown, J. B. Forsyth, and F. Tasset, Solid State Sci. **7**, 682–689 (2005).

[7] R. Nathans, C. G. Shull, G. Shirane, and A. Andersen, J. Phys. Chem. Solids **10**, 138–146 (1959).

[8] M. Blume, Phys. Rev. **133**, A1366 (1963).

[9] P. J. Brown, V. Nunez, F. Tasset, J. B. Forsyth, and P. Radhakrishna, J. Phys.: Condens. Matter **2**, 9409 (1990).

[10] P. J. Brown, *Neutron Scattering from Magnetic Materials*, 1st ed. (Elsevier B.V., The Netherlands, 2006), Chap. 5, pp. 215–244.

[11] R. M. Moon, T. Riste, and W. C. Koehler, Phys. Rev. **181**, 920 (1969).

[12] R. M. Moon, J. Appl. Phys. **41**, 883 (1970).

[13] F. Tasset, Physica B **156**, 627 (1989).

[14] M. T. Rekveldt, J. Phys., Colloq. **32**, C1–C579 (1971).

[15] E. Lelievre-Berna, E. Bourgeat-Lami, Y. Gibert, N. Kernavanois, J. Locatelli, T. Mary, G. Pastrello, A. Petukhov, S. Pujol, R. Rouques, F. Thomas, M. Thomas, and F. Tasset, Physica B **356**, 141 (2005).

[16] N. Qureshi, J. Appl. Cryst. **52**, 175–185 (2019).

[17] M. Takeda, M. Nakamura, K. Kakurai, E. Lelievre-Berna, F. Tasset, and L.-P. Regnault, Physica B **356**, 136 (2005).

[18] M. Janoschek, S. Klimko, R. Gahler, B. Roessli, and P. Boni, Physica B **397**, 125 (2007).

[19] J. Kindervater, W. Haussler, M. Janoschek, C. Pfleiderer, P. Boni, and M. Garst, J. Phys.: Conf. Ser. **89**, 180408 (2014).

[20] T. Wang, S. R. Parnell, W. A. Hamilton, F. Li, A. L. Washington, D. V. Baxter, and R. Pynn, Rev. Sci. Instrum. **87**, 033901 (2016).

[21] V. Hutanu, M. Meven, S. Masalovich, G. Heger, and G. Roth, J. Phys.: Conf. Ser. **294**, 012012 (2011).

[22] L. Crow, W. A. Hamilton, J. K. Zhao, and J. L. Robertson, J. Phys.: Conf. Ser. **746**, 012010 (2016).

[23] W. Chen, T. Gentile, R. Erwin, S. Watson, Q. Ye, K. Krycka, and B. Maranville, J. Phys.: Conf. Ser. **528**, 012014 (2014).

[24] At NCNR, the unpolarized beam can be polarized by other devices, e.g, a supermirror. A ^{3}He polarizer was used for its availability and it not requiring beam collimation.

[25] W. Chen, T. Gentile, C. Fu, S. Watson, G. Jones, J. McIver, and D. Rich, J. Phys.: Conf. Ser. **294**, 012003 (2011).

[26] NFPA 70, National electrical code, National Fire Protection Association, Quincy, Massachusetts, 2010.

[27] C. Elliott, V. Vijayakumar, W. Zink, and R. Hansen, Phys. Rev. B **12**, 17–24 (2007).

[28] This is a Labview™ based software commonly used for scanning probe microscopy (Nanonis GmbH, Zurich, Switzerland). This interface is a result of years of development within an experimental laboratory environment.[29]

[29] J. R. Rodriguez, "Interfacing a Nanonis controller with a scanning tunneling microscope," Ph.D. thesis, Cornell University 2016.

[30] This is a gateless version of the design by Geyger, using a ferrite core.[35–37]

[31] D. H. Clewell, R. A. Broding, G. B. Loper, S. N. Heaps, R. F. Simon, R. L. Mills, and M. B. Dobrin, Rev. Sci. Instrum. **24**, 243 (1953).

[32] W. A. Geyger, Trans. Am. Inst. Electr. Eng., Part 1 **81**, 65–73 (1962).

[33] A. Matsuoka, M. Shinohara, Y.-M. Tanaka, A. Fujimoto, and K. Iguchi, *An Introduction to Space Instrumentation* (TERRAPUB, Japan, 2013), pp. 217–225.

[34] Magnetic Shield Corporation, 740 N. Thomas Drive Bensenville, IL 60106, USA.

[35] W. DeSorbo, Phys. Rev. **132**, 107 (1963).

[36] E. Lelievre-Berna, P. Brown, F. Tasset, K. Kakurai, M. Takeda, and L.-P. Regnault, Physica B **397**, 120 (2007).

[37] J. Tosado, W. Chen, and E. E. Rodriguez, "A strategy for handling aberration in Spherical Neutron Polarimetry," J. Phys.: Conf. Ser. (to be published).